Supplementary Information (SI) for ChemComm.

Sub-grain Boundaries by Cold-Rolling Copper Nanoparticles for Boosting Alkaline HER

Le Shuai,[a] Chuanqi Cheng,*[a,d] Wenxuan Lv,[a] Xinzhuo Hu,[a] Chunyan Han,[a] Zhe Li,[e] Yanzhu Dai,[a,c] Long Shang,[a] Rui Zhang,[a] Cunku Dong,[a] Jing Yang,[a] Hui Liu,[a,b,c] Xi-Wen Du,*[a,b,c] and Peng-Fei Yin*[a,b]

[a.] *Institute of New-Energy Materials, School of Materials Science and Engineering, Tianjin University, Tianjin 300072, China.*

[b.] *State Key Laboratory of Precious Metal Functional Materials, Tianjin University, Tianjin, China*

[c.] *Core Facility Platform, Tianjin University, Tianjin 300354, China*

[d.] *Department of Chemistry, School of Science, Tianjin University, Tianjin 300072, China*

[e.] *Institute of Molecular Plus, School of Chemical Engineering and Technology, Tianjin University, Tianjin 300072, China*

**Corresponding authors*

Emails: tjuccq@tju.edu.cn, xwdu@tju.edu.cn, pengfeiyin@tju.edu.cn

Materials and Methods

Experimental section:

Chemical reagents: Copper powder (99.9%, Zhongke Jinyan (Beijing) Technology Co., Ltd.), potassium hydroxide (KOH, GR, 95%, Shanghai Macklin Biochemical Co., Ltd.), and D_2O (99.9%, DSOURCE Co., Ltd.) were used without further purification. All aqueous solutions were prepared using ultrapure water obtained from a Direct-Q system (18.2 MΩ cm^{-1}), which was also used for cleaning procedures.

Preparation of Cu sample: RNPs and RMPs were fabricated through a cold-rolling strategy. Crystalline Cu nanoparticles (NPs) and microparticles (MPs) with a purity of 99.9% were used as the precursor materials (their initial characterizations are provided in Figs. S1 and S2). Prior to rolling, the powders were thermally treated at 150 °C for 2 h in a mixed 10% H_2/Ar atmosphere to relieve residual stress and eliminate surface oxides accumulated during storage. For the rolling procedure, 5 g of Cu powder (either NPs or MPs) was evenly distributed between two ultrathin stainless-steel sheets that acted as supporting substrates. The stacked configuration was subsequently subjected to deformation using a laboratory-scale electric vertical two-roll mill (TOB-JS-200L). During processing, the thickness reduction was increased by 20% after each rolling pass, and the operation was repeated multiple times. The obtained products were designated as RNPs and RMPs, respectively.

Preparation of TEM lamellae of the RNPs-5 sample: Samples for TEM were prepared using a focused ion beam (FIB) system (Helios 5 UX, Thermo Fisher Scientific) equipped with a Ga^+ ion source operated at 30 kV. Prior to milling, a ~1 μm-thick Pt protective layer was deposited on the region of interest to minimize ion-beam-induced damage during coarse milling. The samples were then thinned via stepwise milling with progressively reduced ion beam currents until electron-transparent thickness was achieved. Finally, the lamellae were lifted out using a micromanipulator and transferred onto a Cu grid for subsequent TEM characterization.

Grain boundary density analysis: Grain boundary (GB) densities were quantified based on electron backscatter diffraction (EBSD) measurements. The samples for EBSD were polished using a Leica EM TIC 3X ion beam milling system. GB distribution maps obtained from EBSD were used for statistical analysis, where grain boundaries were classified according to the misorientation angle into sub-grain boundaries (Sub-GBs, 0-2°), low-angle grain boundaries (L-GBs, 2-10°), and high-angle grain boundaries (H-GBs, 10-180°). The GB density was defined as the total boundary length per unit area in the EBSD mapping region. The boundary length was determined using a pixel-based method by extracting GB traces from the EBSD maps and converting the counted pixels into real lengths according to the EBSD step size, followed by normalization by the analyzed area. Each dataset was obtained from three independent EBSD regions, and the averaged values were reported.

Materials characterizations:

The GB distributions of the samples were analyzed by electron backscatter diffraction (EBSD) and transmission Kikuchi diffraction (TKD) using a focused ion beam scanning electron microscope (FIB-SEM, Helios 5 UX). The morphology and microstructural features of the catalysts were further examined with transmission electron microscopy (TEM, JEOL JEM-F200 and ThermoFisher Talos-F200X) operated at an acceleration voltage of 200 kV.

Phase identification was carried out by X-ray diffraction (XRD, Bruker D8 Advance) employing Cu Kα radiation (λ = 1.5418 Å) with a Ni filter. Surface morphology was also inspected by scanning electron microscopy (SEM, Hitachi S-4800).

The surface chemical states were investigated using X-ray photoelectron spectroscopy (XPS, Thermo Fisher Scientific ESCALAB 250Xi, USA), and the binding energies were calibrated with the C 1s peak at 284.8 eV. Raman spectra were collected on a HORIBA XploRA PLUS confocal Raman microscope with a 532 nm excitation laser.

In addition, the local atomic bonding environment of the Cu samples was probed by X-ray absorption fine structure (XAFS) spectroscopy using a Table XAFS-500-A spectrometer operated in transmission mode at room temperature.

Electrochemical measurements:

All electrochemical measurements were conducted at room temperature using a CHI760E electrochemical workstation. Cyclic voltammetry (CV), linear sweep voltammetry (LSV), and chronoamperometry (i-t) tests were performed to evaluate the electrochemical performance. The HER activity was measured in a standard three-electrode glass cell containing Ar-saturated 1.0 M KOH electrolyte. A saturated Hg/Hg_2Cl_2 electrode (SCE) filled with KCl was used as the reference electrode, while a graphite rod served as the counter electrode. The RNPs-X and RMPs-X samples were directly used as self-supported electrodes for alkaline HER measurements.

The potential measured versus SCE were calibrated to reversible hydrogen electrode (RHE) based on the Nernst equation:

$$E_{\mathrm{RHE}}(\mathrm{V}) = E_{\mathrm{SCE}}(\mathrm{V}) + 0.242\ \mathrm{V} + 0.0592\ \mathrm{V} \times \mathrm{pH}_{\mathrm{electrolyte}}$$

The HER polarization curves were collected using linear sweep voltammetry (LSV) with a scan rate of 5 mV s^{-1}. A long-term stability test was carried out using chronoamperometry under the overpotential of 0.5 A cm^{-2}.

Electrochemical active surface area: The electrochemically active surface area (ECSA) was estimated from the double-layer capacitance (C_{dl}) obtained in the non-Faradaic region. Cyclic voltammetry (CV) measurements were conducted at scan rates of 10-90 mV s^{-1}. The capacitive current density, $\Delta j = (j_a - j_c) / 2$ at 0.70 V vs. RHE, was plotted against the scan rate, and the slope was taken as C_{dl}. The ECSA was calculated using：

$$\mathrm{A}_{\mathrm{ECSA}} = \frac{C_{\mathrm{dl}}}{C_s}$$

where C_s represents the specific capacitance of a flat surface and was assumed to be 40 μF cm^{-2}.

Electrochemical in-situ Raman spectra measurements: In situ electrochemical Raman measurements were performed using a HORIBA XploRA PLUS Raman microscope with a 532 nm excitation laser, while the electrode potential was controlled by an electrochemical workstation. A Teflon electrochemical cell fitted with a circular quartz window was employed to allow laser irradiation and to protect the sample during measurements. The working electrode was positioned parallel to the quartz window so that the sample surface remained perpendicular to the incident laser beam. A Pt wire was shaped into a ring surrounding the working electrode and used as the counter electrode. A KCl-saturated Hg/Hg_2Cl_2 electrode served as the reference electrode, and 1.0 M KOH was used as the electrolyte. Potentials ranging from the open-circuit potential (OCP) to -0.4 V vs. RHE were sequentially applied, with each potential held for 300 s to reach stabilization. Raman spectra were subsequently collected under operando conditions while maintaining potentiostatic control.

Computational details:

In this work, all DFT calculations were performed using the Vienna Ab initio Simulation Package (VASP). The projector augmented wave (PAW) pseudopotential with the PBE generalized gradient approximation (GGA) exchange correlation function was utilized in the computations. The cut-off energy of the plane wave basis set was 500 eV, and a Monkhorst-Pack mesh of 3×3×1 was used for K-sampling in the adsorption energy calculation. The long-range dispersion interaction was described by the DFT-D3 method. The electrolyte was incorporated implicitly with the Poisson-Boltzmann model implemented in VASPsol++. The relative permittivity of the media was chosen to be $\varepsilon_r = 78.4$, corresponding to that of water. The Debye length for the electrolyte was set to 3.0 Å, which corresponds to an electrolyte concentration of 1.0 M. All atoms were fully relaxed with an energy convergence tolerance of 10^{-5} eV per atom, and the final force on each atom was < 0.01 eV Å^{-1}. The TS searches were performed using the climbing-image nudged elastic band (CI-NEB) and the Dimer method in the VTST package. The final force on each atom was < 0.05 eV Å^{-1}. The TS search is conducted by using the CI-NEB method to generate initial guess geometries, followed by the dimer method to converge to the saddle points. For the *ab-initio* molecular dynamics (AIMD) simulations, canonical ensemble (NVT) conditions were imposed by a Nose-Hoover thermostat with a target temperature of 300 K. The MD time step was 1 *fs*, and all the systems were run for 10 *ps* to reach equilibrium. For the model construction, we selected a Cu bulk model constructed with three basis vectors: (111), (1 10), and (11 2). The dislocation model was built by removing half a layer of the (111) crystal planes, and the model was subsequently relaxed through AIMD simulations and DFT calculations. The adsorption model was obtained by slicing the relaxed bulk model along the (111) plane.

The adsorption energy of reaction intermediates, can be computed using the following Equation (1)-(2):

$$\Delta E = E(_{\mathrm{ads/slab}}) - E_{\mathrm{ads}} - E_{\mathrm{slab}} \tag{1}$$

$$\Delta G = \Delta E + \Delta E_{\mathrm{ZPE}} - \mathrm{T}\Delta S \tag{2}$$

Where ΔE_{ZPE} is the zero-point energy change, ΔS is the entropy change. In this work, the values of ΔE_{ZPE} and ΔS are obtained by vibration frequency calculation.

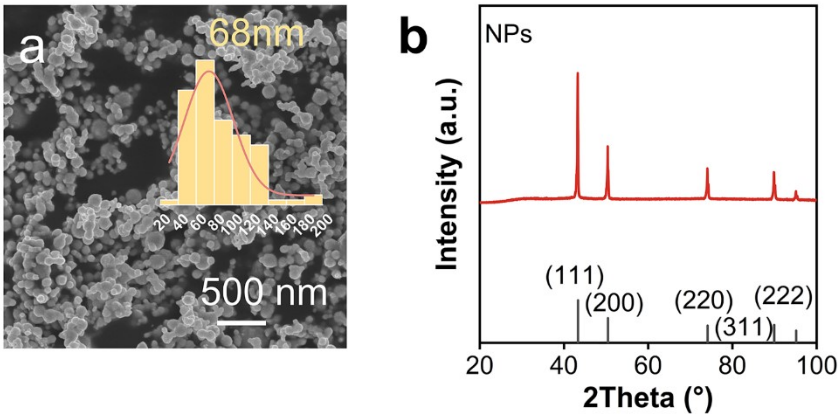

Fig. S1 (a) SEM image of pure Cu NPs with the corresponding particle size distribution (inset). (b) XRD pattern of pure Cu NPs.

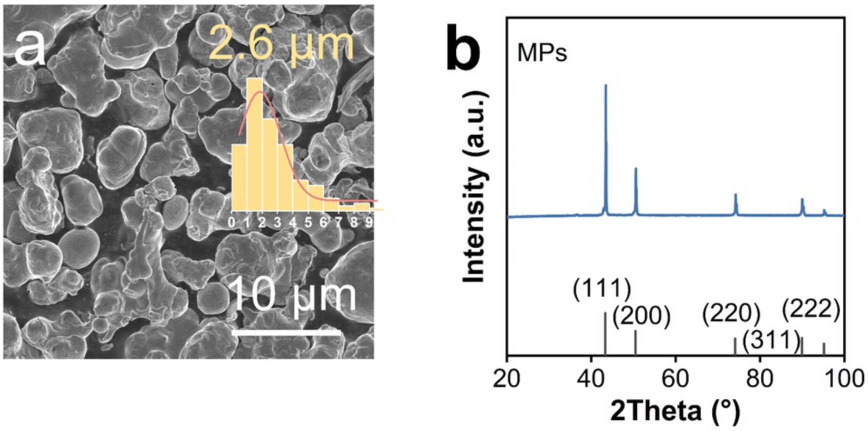

Fig. S2 (a) SEM image of pure Cu MPs with the corresponding particle size distribution (inset). (b) XRD pattern of pure Cu MPs.

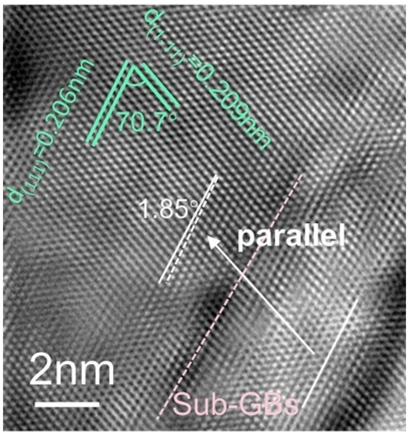

Fig. S3 Inverse Fast Fourier Transform (IFFT) image derived from Fig. 2d showing a lattice rotation of ~1.85° across a representative Sub-GB.

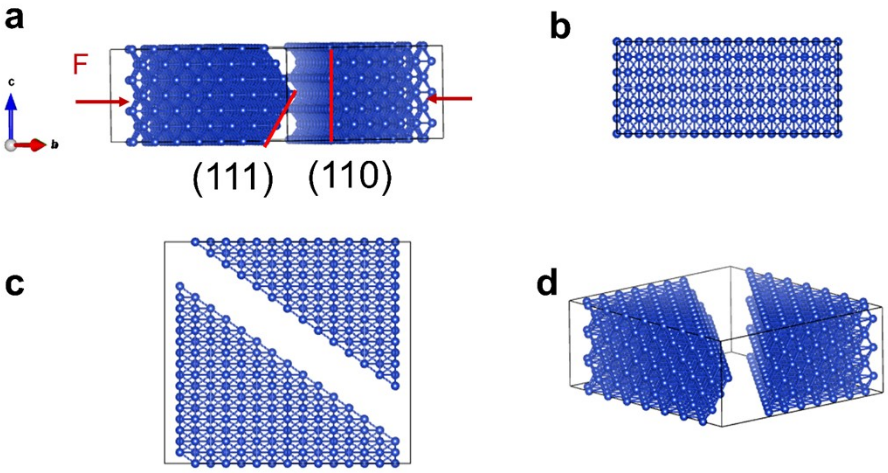

Fig. S4 Initial Cu (111)-Cu (110) interface models for AIMD simulation. (a-d) Models from different perspectives, the arrows represent the direction of force.

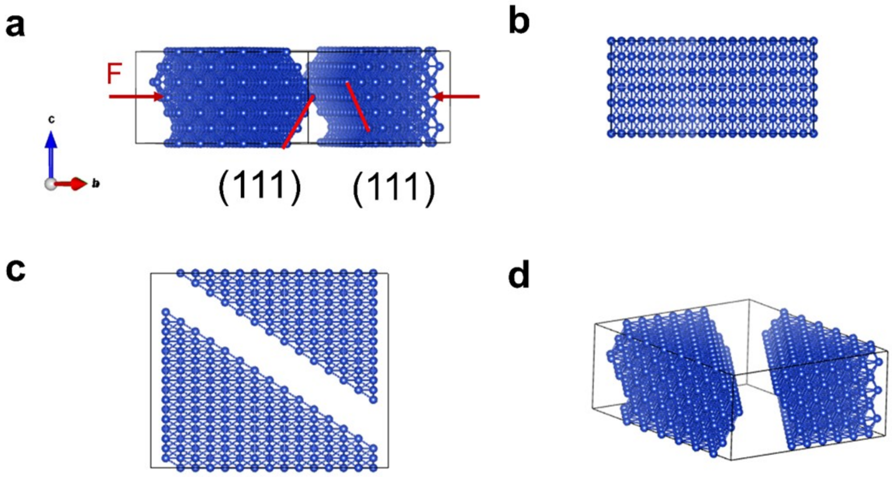

Fig. S5 Initial Cu (111)-Cu (111) interface models for AIMD simulation. (a-d) Models from different perspectives, the arrows represent the direction of force.

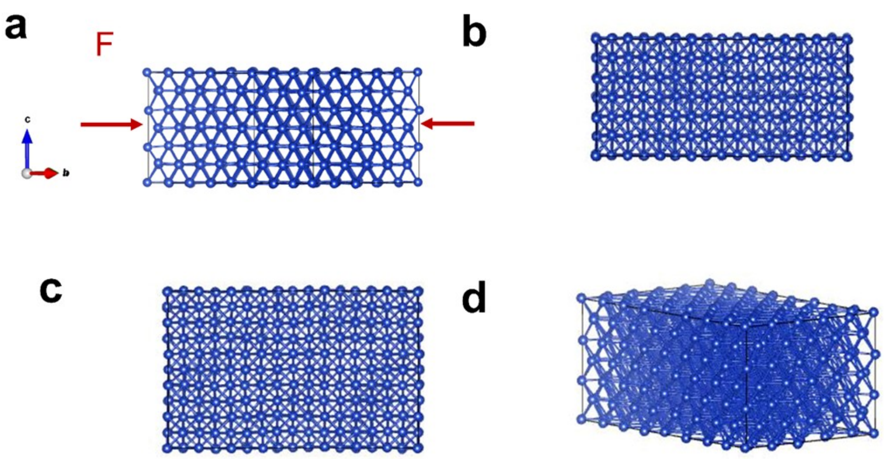

Fig. S6 Initial single crystalline Cu grain model for models. (a-d) Model from different perspectives, the arrows represent the direction of force.

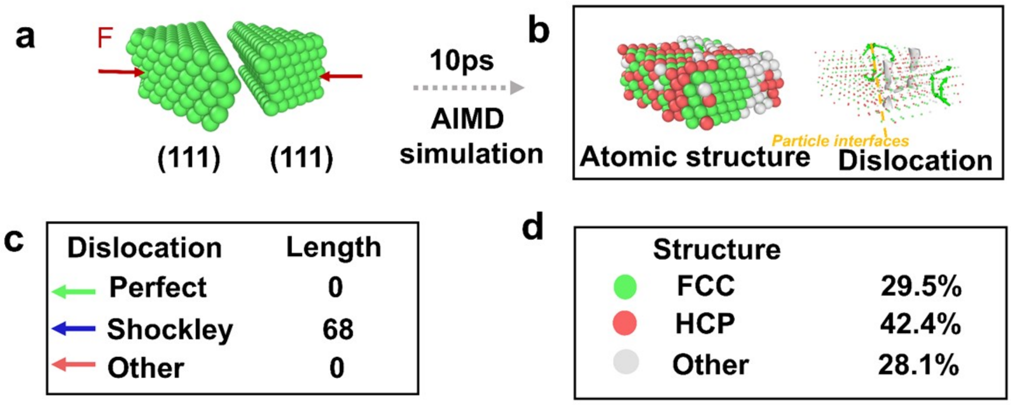

Dislocation	Length
← Perfect	0
← Shockley	68
← Other	0

Structure	
● FCC	29.5%
● HCP	42.4%
● Other	28.1%

Fig. S7 AIMD-derived deformation evolution of two Cu (111)-(111) particles under compression. (a) initial structure. (b) AIMD snapshots illustrating the structural evolution of Cu under opposite compression along the red arrows for 10 *ps*, showing atomic configuration (left) and dislocation distribution (right). The arrows represent the dislocation Burgers vector. (c) Table summarizes the final lattice. (d) Table summarizes the total dislocation lengths.

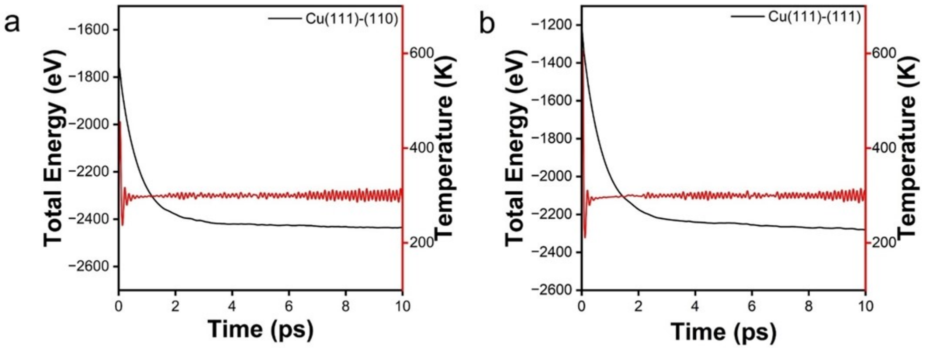

Fig. S8 Time evolution of the total energy and temperature of the system during the AIMD simulation: (a) Cu(111)-Cu(110) interface, (b) Cu(111)-Cu(111) interface.

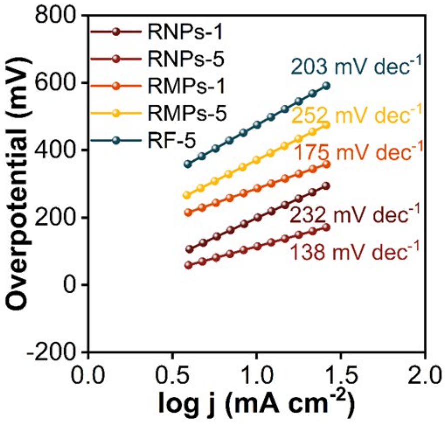

Fig. S9 Tafel slopes of RNPs, RMPs, and RF with varying rolling passes.

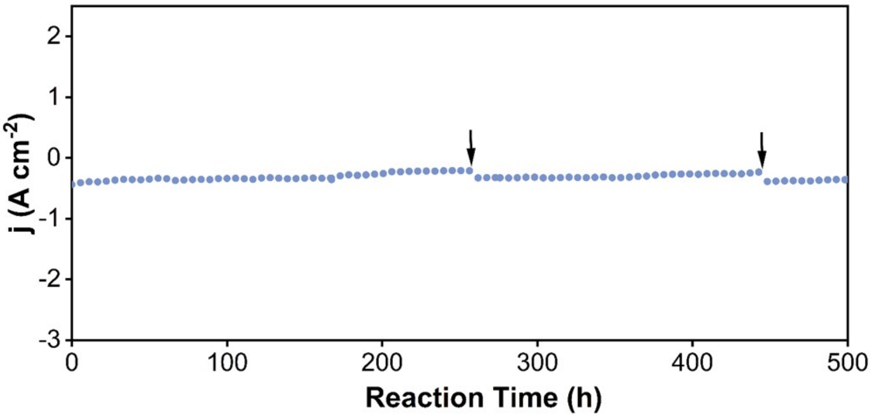

Fig. S10 Long-term stability of RNPs-5 at an initial current density of 0.5 A cm^{-2}.

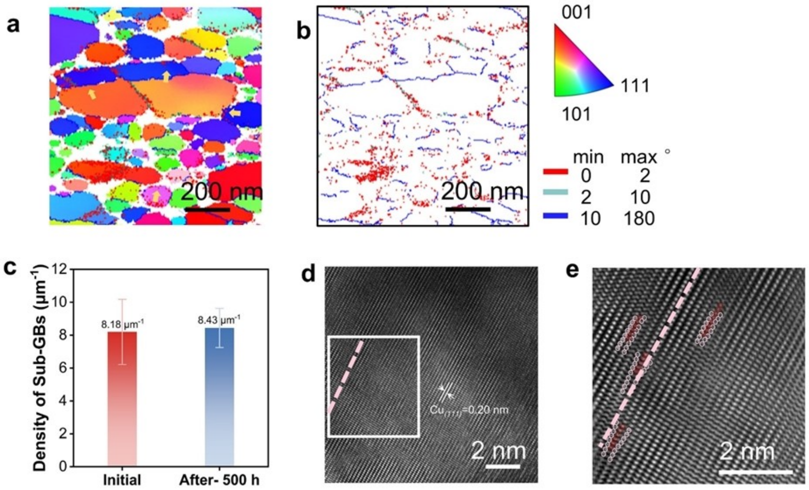

Fig. S11 (a-b) EBSD analysis of RNPs-5 after-500 *h*: (a) IPF map. (b) GB distribution map. (c) Bar chart comparing sub-grain boundary density in RNPs-5 before and after electrochemical stability testing. (d) HRTEM images of RNPs-5 after-500 *h*. (e) IFFT image of the boxed region in the HRTEM image shown in (d), mark the position of Sub-GBs with dashed lines.

Note S1

To quantitatively evaluate the stability of the Sub-GBs, EBSD statistical analysis was conducted after the durability test (Fig. S11 a-b). As summarized in Fig. S11c, the Sub-GB density shows no obvious decrease after long-term HER operation. Moreover, as shown in Fig. S11 d-e, Sub-GB structures remain clearly observable near the particle edges in the HRTEM images, indicating that these interfacial structures are well preserved even under prolonged high-current-density operation. These results collectively confirm the excellent structural stability of the Sub-GB-rich catalyst during long-term HER electrolysis.

Table S1 Summary on HER properties of Cu electrocatalysts.

Catalysts	Overpotential (mV @ 10 mA cm^{-2})	Tafel(mV dec^{-1})	Stability (h)	Reference
RNPs-Cu	116	138	(500 mA cm^{-2}) 500	This work
DNTs-Cu	61	33	(500 mA cm^{-2}) 125	[1]
Ag@Cu_2O/Cu	108	58	(27 mA cm^{-2}) 20	[2]
Cu_3N/NF	118	122	(10 mA cm^{-2}) 14	[3]
Cu@WC	119	50.5	(10 mA cm^{-2}) 12	[4]
PS-Cu	121	144	(100 mA cm^{-2}) 30	[5]
Cu@NC NT/CF-500	123	61	(10 mA cm^{-2}) 10	[6]
FSW-FeCu-E	142	113	(1 A cm^{-2}) 20	[7]
CuFe	153	36	(-0.33 V vs. RHE) 150	[8]
F-Cu/NF	183	325	(100 mA cm^{-2}) 100	[9]

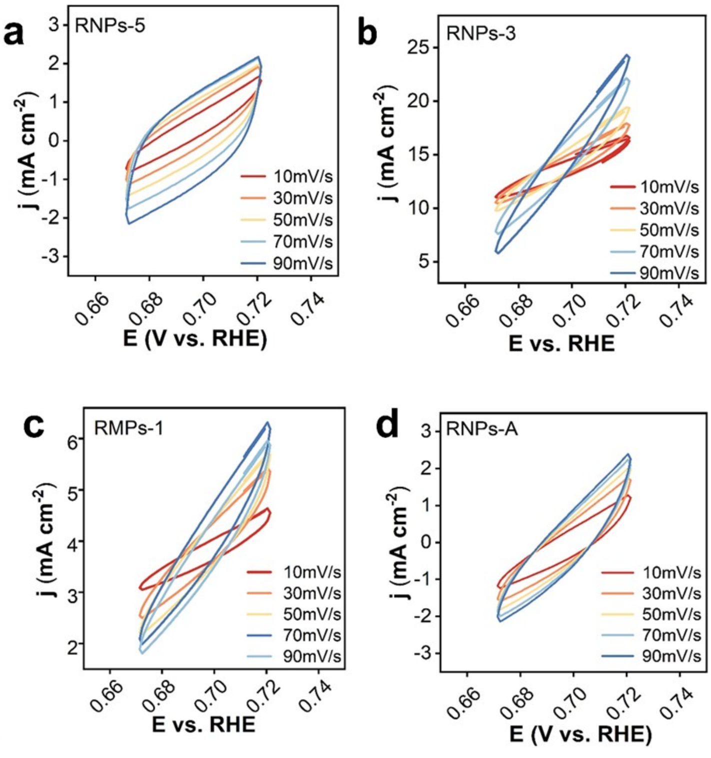

Fig. S12 (a-d) CV curves of different samples recorded at scan rates of 10, 30, 50, 70, and 90 mV s^{-1} in 1 M KOH.

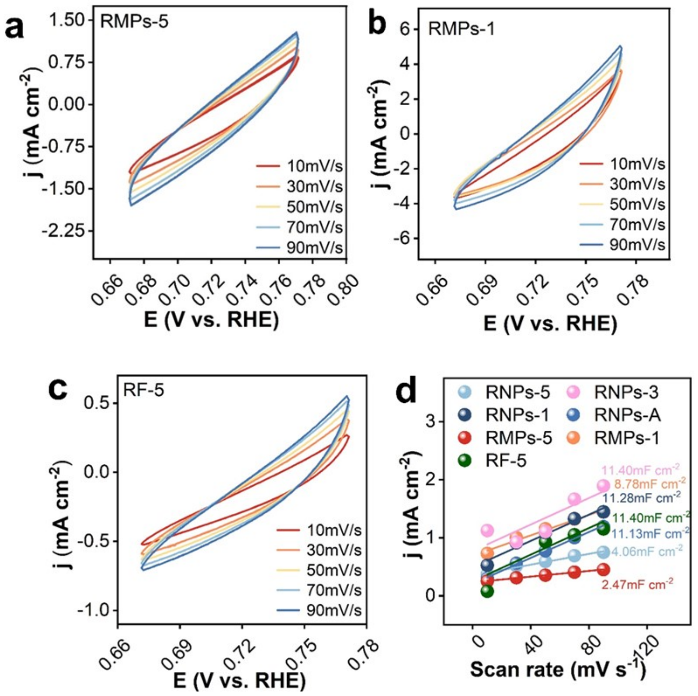

Fig. S13 (a-c) CV curves of different samples recorded at scan rates of 10, 30, 50, 70, and 90 mV s^{-1} in 1 M KOH. (d) C_{dl} values derived from linear fitting of the current density versus scan rate plots shown in Fig. S12 and Fig. S13a-c.

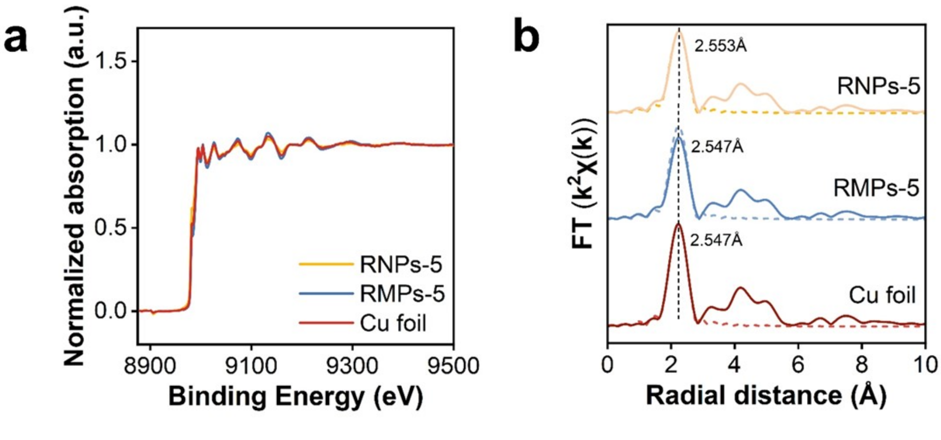

Fig. S14 XAFS spectra of RNPs-5, RMPs-5, and the Cu foil reference: (a) Cu K-edge XANES spectra; (b) Fourier-transformed EXAFS spectra.

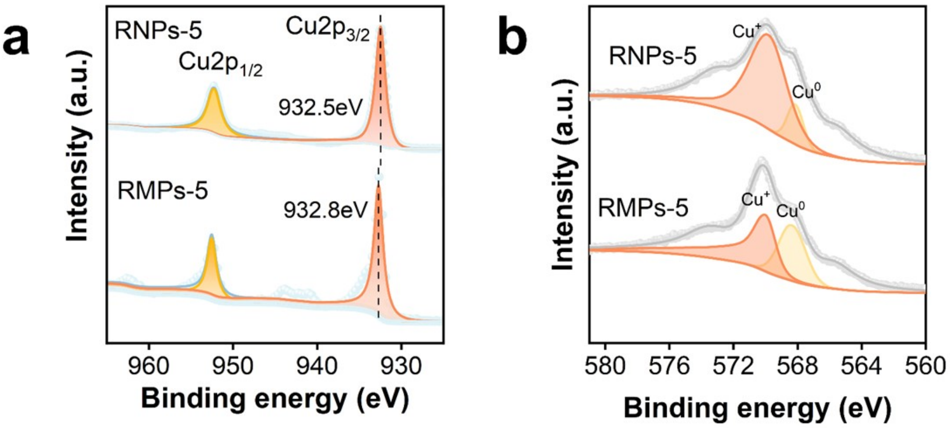

Fig. S15 XPS spectra of RNPs-5 and RMPs-5. (a) High-resolution Cu 2p spectra. (b) Cu LMM Auger spectra.

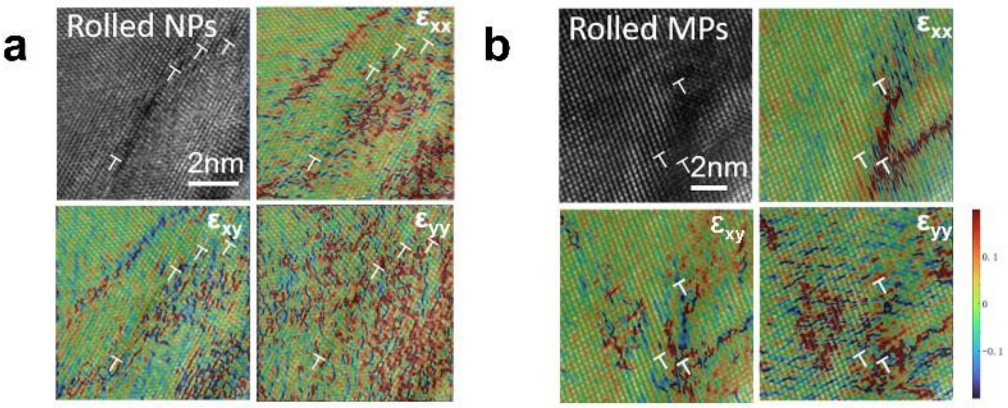

Fig. S16 Geometric phase analysis (GPA) strain mappings of (a) RNPs-5 and (b) RMPs-5.

Note S2 Valence state and strain analysis of RNPs-5 and RMPs-5

EXAFS spectra (Fig. S14) show that, for both NPs and MPs, the Cu-Cu bond lengths after rolling are comparable to the Cu foil reference, indicating the absence of lattice distortion or macroscopic strain.

XPS results (Fig. S15) indicate that, despite slight surface oxidation, the dominant Cu^0 signals in both samples remain clear with no peak shift, reflecting similar valence states.

GPA analysis of the Sub-GB regions (Fig. S16) reveals comparable local strain distributions, with tensile and compressive strains appearing in paired forms.

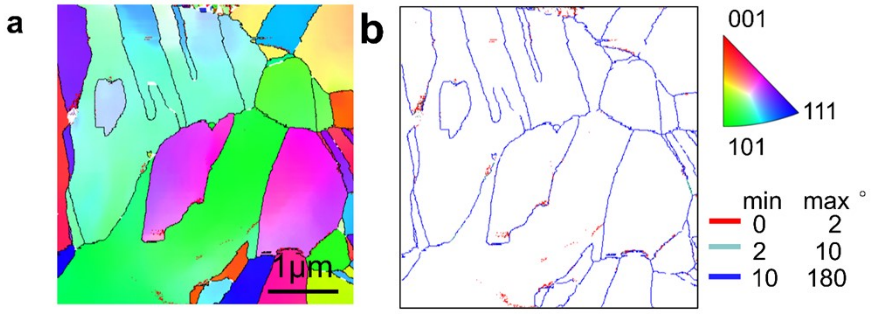

Fig. S17 EBSD analysis of RNPs-A. (a) IPF map. (b) GB distribution map.

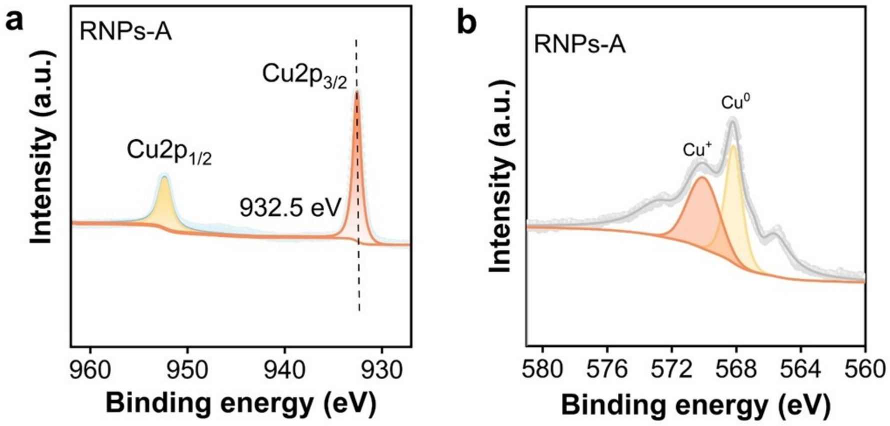

Fig. S18 XPS spectra of RNPs-A. (a) High-resolution Cu 2p spectra. (b) Cu LMM Auger spectra.

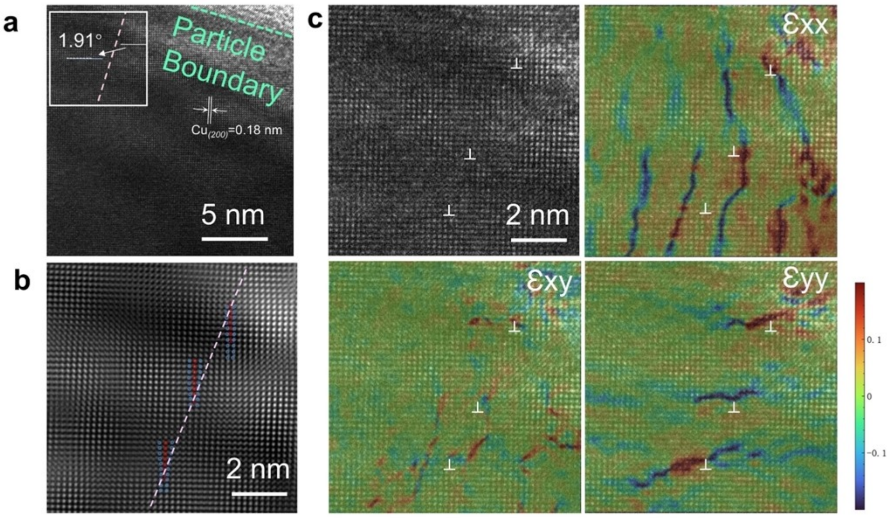

Fig. S19 (a) HRTEM images of RNPs-A. (b) IFFT image of the boxed region in the HRTEM image shown in (a), mark the position of Sub-GBs with dashed lines. (c) Geometric phase analysis (GPA) strain mappings of the boxed region in the HRTEM image shown in (a).

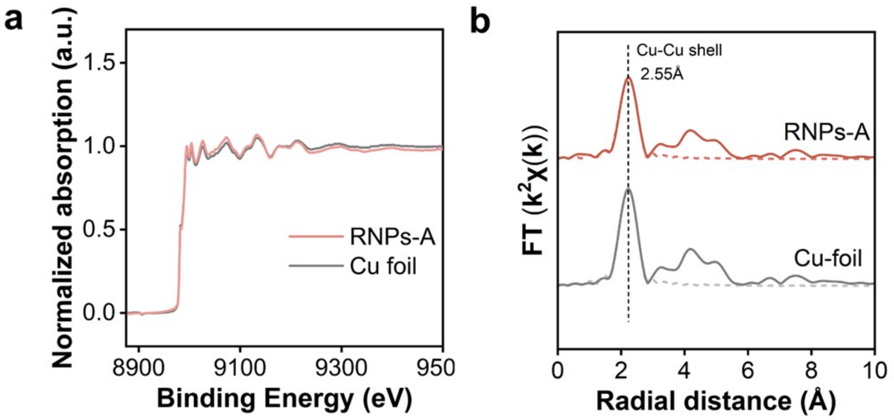

Fig. S20 XAFS spectra of RNPs-A and the Cu foil reference: (a) Cu K-edge XANES spectra; (b) Fourier-transformed EXAFS spectra.

Note S3 Valence state and strain analysis of RNPs-A

XPS results confirm that the annealed samples are still dominated by Cu^0/Cu^+ species (Fig. S18), excluding significant changes in surface valence states as the primary origin of the activity variation.

AIMD simulations indicate that strain in cold-rolled nanoparticles is mainly accommodated via dislocations, leading to localized stress around dislocation cores and Sub-GBs. Annealing reduces defect density (Sub-GB density decreases to ~0.57 μm^{-1}) through dislocation motion and annihilation, but primarily reduces the number of stressed regions rather than significantly altering the local stress state. This is supported by GPA (Fig. S19), which shows negligible change in local strain intensity near remaining defects, and EXAFS (Fig. S20), which reveals no appreciable change in Cu-Cu coordination features.

Overall, although annealing induces some degree of grain growth (Fig. S17) and decreases the defect density, neither the surface valence state nor the local stress state changes significantly.

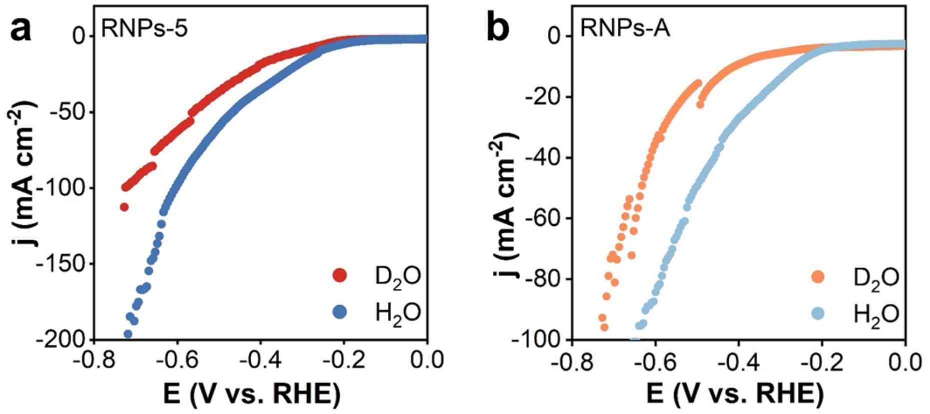

Fig. S 21 HER polarization curves measured in 1 M KOH prepared with H_2O and D_2O of (a) RNPs-5 and (b) RNPs-A.

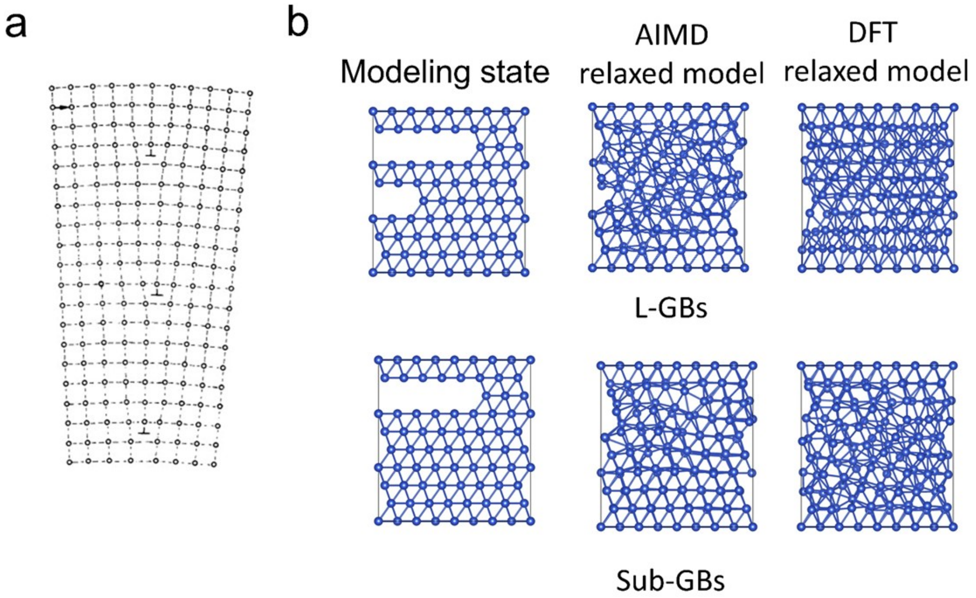

Fig. S 22 (a) Schematic illustration of the L-/Sub- GBs. (b) Atomic models of the L-GBs and Sub-GBs constructed for theoretical calculations.

Note S4:

The structural models in Fig. S22 were developed based on experimental observations and classical dislocation grain boundary theory, in an effort to reasonably capture the structural characteristics of Sub-GBs and L-GBs.

From a crystallographic perspective, both Sub-GBs and L-GBs can be regarded as ordered dislocation arrays (Fig. S22a).[10] However, Sub-GBs possess much smaller misorientation angles, resulting in significantly larger dislocation spacings. HRTEM analysis shows that adjacent dislocation cores within the Sub-GBs are separated by at least ~10 lattice planes (Fig. 2e, Fig. S11d and Fig. S19b).

In contrast, the strongly distorted region surrounding an individual dislocation core is typically confined within ~1 nm (~5-6 atomic layers),[11] which is also supported by our GPA analysis (Fig. S16). Since this interaction range is much smaller than the spacing between neighboring dislocations in the Sub-GBs, the interactions among dislocations are relatively weak. Therefore, a simplified single-dislocation model was used to represent the Sub-GB structure.

According to the classical Read-Shockley theory,[12] L-GBs accommodate larger crystallographic misorientations and thus possess much shorter dislocation spacings, where dislocation interactions can no longer be neglected. Accordingly, a multiple-dislocation model was adopted for the L-GB structure.

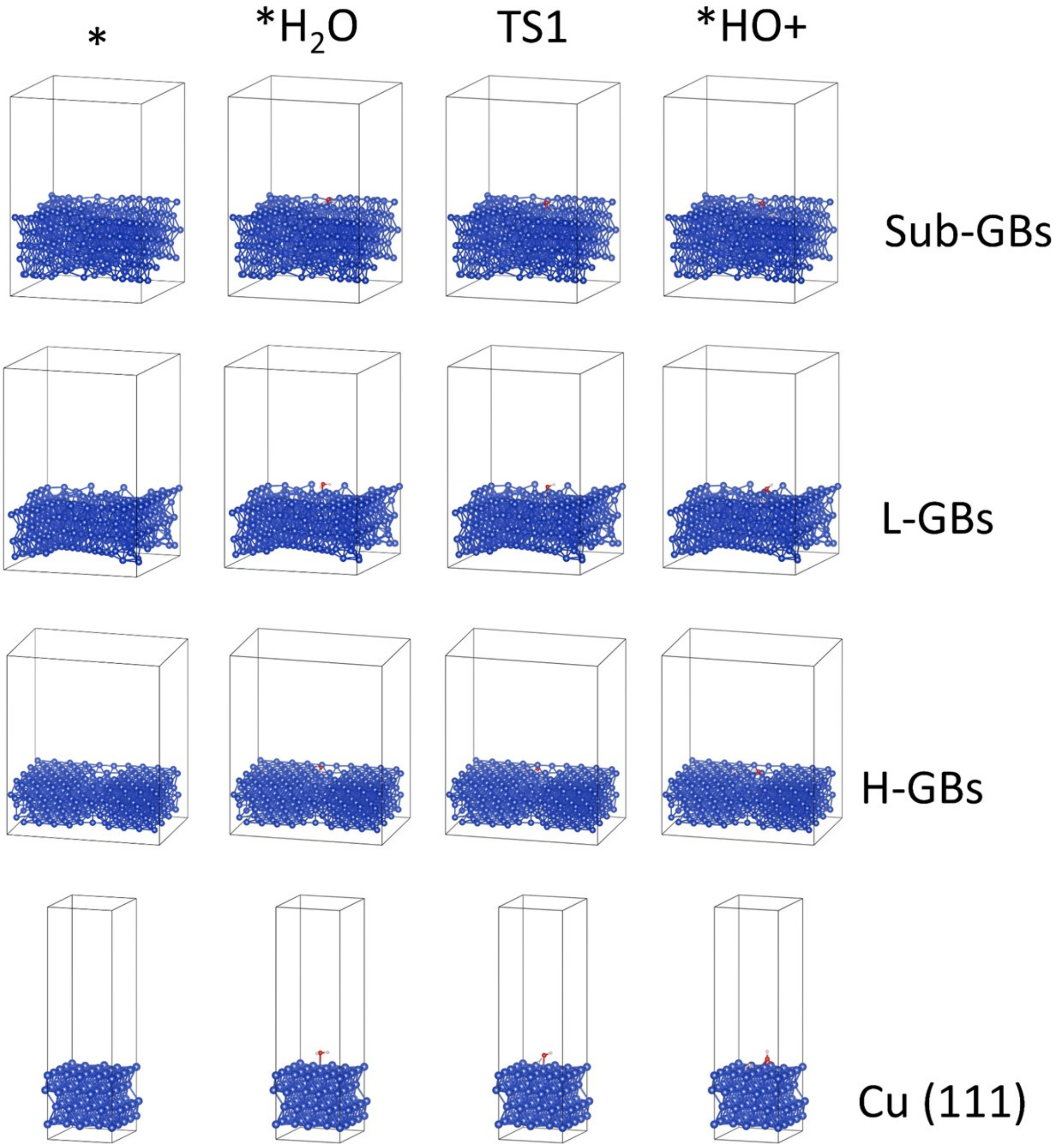

Fig. S 23 Atomic models of H_2O adsorption and dissociation on the ideal Cu (111) surface, Sub-GBs, L-GBs, and H-GBs used for the DFT calculations.

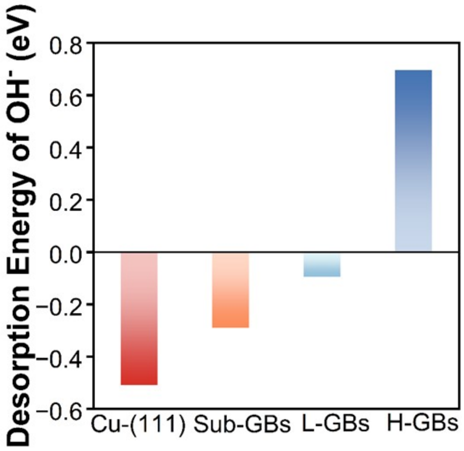

Fig. S24 Comparison of OH* desorption energies on different grain boundary models.

Note S5

As shown in Fig. S24, all grain-boundary models exhibit higher OH desorption energies relative to Cu(111), indicating that grain-boundary structures generally enhance the interaction with OH intermediates. Notably, while the H-GB model suffers from excessively strong OH binding that imposes a prohibitively high desorption barrier, the OH desorption processes on both the sub-GB and L-GB models remain thermodynamically favorable. For weak hydrogen-binding metals such as Cu, the rate-determining step of alkaline HER is typically water dissociation rather than OH^- or H_2 desorption,[13] and thus the moderately strengthened OH binding on sub-GBs is unlikely to hinder the overall HER process.

Taken together, these results demonstrate that sub-GBs can simultaneously promote water activation and maintain moderate OH* binding strength, thereby striking a favorable balance between intermediate activation and product desorption, an attribute beneficial to the overall HER kinetics.

Reference

1 Z. Li, Y. Wang, H. Liu, Y. Feng, X. Du, Z. Xie, J. Zhou, Y. Liu, Y. Song, F. Wang, M. Sui, Y. Lu, F. Fang and D. Sun, *Nat. Mater.*, 2025, **24**, 424-432.

2 C. Song, Z. Zhao, X. Sun, Y. Zhou, Y. Wang and D. Wang, *Small*, 2019, **15**, 1804268.

3 C. Panda, P. Menezes, M. Zheng, S. Orthmann and M. Driess, *ACS Energy Lett.*, 2019, **4**, 747-754.

4 M. Yao, B. Wang, B. Sun, L. Luo, Y. Chen, J. Wang, N. Wang, S. Komarneni, X. Niu and W. Hu, *Appl. Catal. B Environ.*, 2021, **280**, 119451.

5 W. Kang, Y. Feng, Z. Li, W. Yang, C. Cheng, Z. Shi, P. Yin, G. Shen, J. Yang, C. Dong, H. Liu, F. Ye and X. Du, *Adv. Funct. Mater.*, 2022, **32**, 2112367.

6 Y. Zhang, Y. Ma, Y. Chen, L. Zhao, L. Huang, H. Luo, W. Jiang, X. Zhang, S. Niu, D. Gao, J. Bi, G. Fan and J. Hu, *ACS Appl. Mater. Interfaces*, 2017, **9**, 36857-36864.

7 L. Ji, Y. Feng, C. Cheng, Z. Li, W. Guan, B. He and Z. Liu, *Small*, 2022, **18**, 2107481.

8 J. Li, C. Han, J. Zhang, P. Yin and X. Du, *Langmuir*, 2025, **41**, 4730-4735.

9 Y. Tang, C. Fan, Z. Zang, Y. Cheng, L. Li, X. Yu, X. Yang, Z. Lu, X. Zhang and H. Liu, *J. Colloid Interface Sci.*, 2025, **683**, 312-321.

10 R. Cahn and P. Haasen, in *Physical Metallurgy*, North-Holland, 1996, pp. 843-942.

11 R. M. J. Cotterill and M. Doyama, *Phys. Rev.*, 1966, **145**, 465-478.

12 W. T. Read and W. Shockley, *Phys. Rev.*, 1950, **78**, 275-289.

13 Q. Wu, M. Luo, J. Han, W. Peng, Y. Zhao, D. Chen, M. Peng, J. Liu, F. M. F. de Groot and Y. Tan, *ACS Energy Lett.*, 2020, **5**, 192-199.